New method of out-of-time energy subtraction for the CMS hadronic calorimeter

IOP Conf. Series: Journal of Physics: Conf. Series 1162 (2019) 012036 doi:10.1088/1742-6596/1162/1/012036

New method of out-of-time energy subtraction for the CMS hadronic calorimeter

Jay Lawhorn on behalf of the CMS HCAL Collaboration
California Institute of Technology
E-mail: jlawhorn@caltech.edu

Abstract. The CMS hadronic calorimeter employs plastic scintillator active material in the barrel and endcap (HBHE). In Run 2, the LHC operates at 13 TeV center-of-mass energy with up to 50 simultaneous collisions per bunch crossing (pileup) and a 25 ns bunch spacing. The HBHE scintillator light pulse is only 60% contained in a 25 ns window, resulting in significant pulse overlap for consecutive events (out-of-time pileup). This talk presents a novel algorithm that will be used in 2018 for subtracting out-of-time pileup in HBHE both online in the software trigger and offline. The algorithm includes methods for both the barrel with hybrid photodiode photosensors and QIE8 digitizers, and the endcap with silicon photomultipliers and QIE11 digitizers, including the challenging charge-dependent pulse shaping effects of the QIEs. The on-detector pulse shape measurement method and results are also shown. The new algorithm is five-to-ten times faster than the previous one, and for the first time CMS will use the offline method at the trigger level.

1. Introduction

The CMS hadron calorimeter (HCAL) system is composed of a brass and scintillator calorimeter with a central barrel ($|\eta| \leq 1.6$), and two endcaps ($1.6 \leq |\eta| \leq 3.0$), steel and quartz fiber forward calorimeters ($3.0 \leq |\eta| \leq 5.2$), and an additional outer calorimeter in the the barrel region. A more detailed description of the overall CMS detector can be found in [1], and the HCAL in [2].

Both the barrel (HB) and endcap (HE) detectors consist of alternating layers of brass and plastic scintillator tiles, segmented in η and ϕ as 0.087×0.087 for $|\eta| \leq 1.6$ and 0.17×0.17 for $|\eta| \geq 1.6$. The scintillation light from each tile is collected by a Y11 wavelength-shifting fiber and transmitted to the front-end readout electronics.

In HB, the readout electronics consist of hybrid photo-diodes (HPD) with QIE8 charge-integrating analog-to-digital converters (ADC). In the 2018 HE, the HPD and QIE8 were upgraded to silicon photo-multipliers (SiPM) and QIE11. The QIE chips integrate and digitize the photosensor signal in 25 ns time slices (TS), corresponding to the nominal LHC collision rate. Additionally, the QIE11 includes a rising edge time-to-digital converter (TDC) with 500 ps resolution for each TS. For each channel, three pre-samples and four post-samples are recorded in addition to the TS corresponding to the bunch crossing of interest, for a total of eight stored TS.

The response time of the HB and HE is of the same order as the LHC bunch spacing, dominated by the scintillator and wavelength-shifting fiber response. The energy from a single collision is approximately 60% contained in the corresponding TS, with a further 25% falling into the next TS, and the remaining 15% into later TSs. There is significant overlap between

signals in consecutive collisions, referred to as out-of-time pileup (OOTPU), which significantly degrades physics performance if no mitigation is applied.

Section 2 reports an on-detector measurement of the pulse shape with SiPM and QIE11 readout. Section 3 documents the energy reconstruction used for OOTPU mitigation during the 2018 data taking period. Section 4 details some measures of object-level performance.

2. Pulse shape measurement

The time profile of the HBHE signal response, or pulse shape, for a single channel is determined by the hadronic shower, the scintillation process in the tiles, the optical transmission and wavelength-shifting, the photosensors, and the QIE chips. The QIE chip response in particular has a dependence on input current from the photosensor, due to slew-rate limitations. This distortion effect is adequately modeled as a simple time delay for the purposes of HBHE event reconstruction. Other pulse shape fluctuations are also modeled as time delays, though this is only a parameterization and not a definitive statement on the nature of these fluctuations.

This time delay model requires a relatively granular understanding of the output pulse shape. In normal operations, each channel has a programmable phase delay applied to correct for geometric effects and align the average pulse arrival times. However, in order to measure a pulse shape in bins finer than 25 ns, data at different arrival times is needed.

For the HPD and QIE8 readout chain, the average pulse shape was measured with a 300 GeV pion test beam in 2004-2006 [2]. In that case, the detector readout was asynchronous to the beam arrival, and an external detector provided relative timing information, allowing for sampling the pulse shape through the full range of relative phases.

For the SiPM and QIE11 readout chain, on-detector phase scans were performed instead. During isolated bunch collisions, the programmable phase delay was cycled through 25 different values, with 1 ns spacing. The first on-detector pulse shape measurement with the SiPM readout was made using the 2017 HE pilot wedge [3] and this exercise was repeated for the fully upgraded HE in 2018. The resulting data was sorted by rising-edge TDC value with 1 ns granularity and the unit-normalized pulse shape for all hits with total charge above 30 pC in that range was calculated. Selected average pulse shapes with 5 ns differences in rising edge TDC value are shown in Figure 1.

The differencing method from the 2004-2006 test beams [2] was used to calculate the 1 ns granularity pulse shapes. For the nanosecond window i, the average pulse shape value is

$$q_i = \mathrm{TS}(\lfloor i/n \rfloor, i \bmod n) - \mathrm{TS}(\lfloor (i-1)/n \rfloor, (i-1) \bmod n) + q_{(i-n)} \tag{1}$$

where $0 \leq i < mn$, $m = 8$ is the number of time slices, and $n = 25$ is the number sub-slices per time slice, and $\mathrm{TS}(a, b)$ corresponds to TSa with TDC value corresponding to bin b. The first two terms are the difference of pulse shapes with consecutive arrival times. Considering q_i as the charge migrating into the given TS from the next TS, the $q_{(i-n)}$ term is the charge migrating out of the given TS into the previous one.

To illustrate in the simplified case of 5 ns intervals ($m = 8$, $n = 5$), consider Figure 1. The first non-zero entry is

$$q_{15} = \mathrm{TS}(\lfloor 15/5 \rfloor, 15 \bmod 5) = \mathrm{TS}(3, 0) \tag{2}$$

and $\mathrm{TS}(3, 0)$ corresponds to the TS3 value from the TDC40 pulse. All other terms are zero. Then the next entry is

$$q_{16} = \mathrm{TS}(3, 1) - \mathrm{TS}(3, 0) \tag{3}$$

which is the difference in TS3 from TDC40 to TDC30. The last term is still zero.

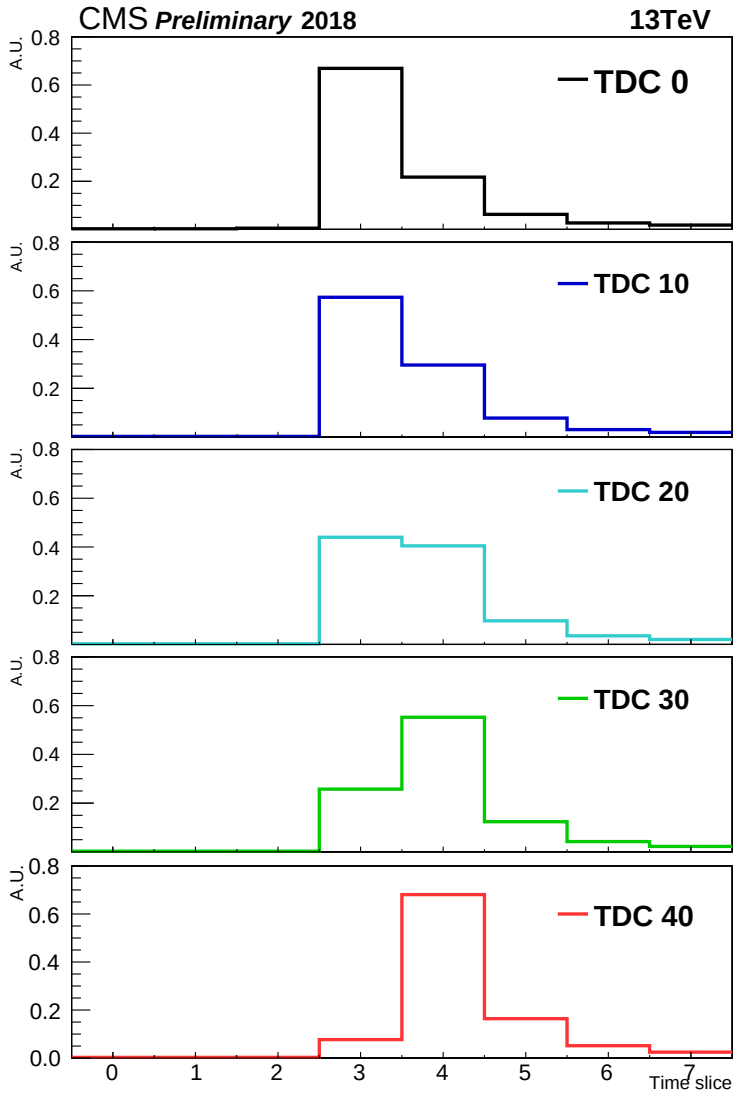

Figure 1. Average unit-normalized pulse shape for selected TDC values. Each TDC count corresponds to 500 ps, so there is a relative shift of 5 ns between each plotted distribution. On the x axis, each time slice (TS) corresponds to 25 ns, with arbitrary scale for the y axis.

Skipping ahead, the fifth non-zero term is

$$q_{20} = \mathrm{TS}(4,0) - \mathrm{TS}(3,4) + q_{15} = \mathrm{TS}(4,0) - \mathrm{TS}(3,4) + \mathrm{TS}(3,0) \tag{4}$$

corresponding to the difference between the TS4 value from the TDC40 pulse and the TS3 value of the TDC0 pulse, with the addition of the TS3 value of the TDC40 pulse.

The 1 ns pulse shape measured from the 2018 phase scan is shown in Figure 2, with the Landau function template used in local reconstruction overlaid. The Landau function parameters are from a fit to the 2017 phase scan data, and are consistent with the higher statistics 2018 phase scan.

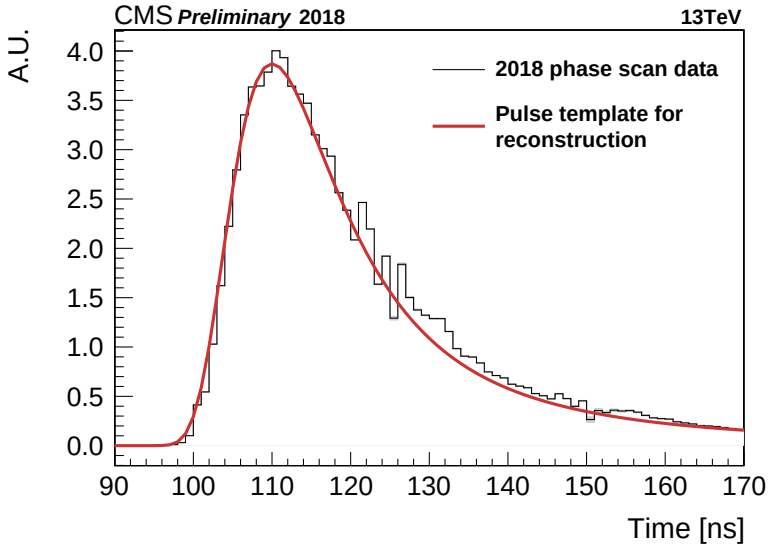

Figure 2. Pulse shape in 1 ns increments. The y axis is in arbitrary units. The black histogram was measured from a 2018 HE phase scan during single bunch collisions. The red distribution is the pulse shape template used for SiPM channels in the HE local reconstruction, and was derived from 2017 phase scans with single bunches.

3. Energy reconstruction

To reconstruct the in-time energy deposit, we perform a two-step template fit for a flat baseline term and up to three pulses. The first try has a flat baseline term and a single pulse in the bunch crossing of interest. If that fit result is poor, a second try with the baseline term and three pulses in the bunch crossing of interest, the previous bunch crossing, and the next bunch crossing is performed. This logic was optimized to minimize CPU time in cases where a single pulse fit and a three pulse fit give compatible answers. This fit is used in both offline reconstruction and online at the software trigger level for the 2018 data taking period.

The pulse shape template p_i is calculated using the previously described pulse shape measurement and a linear translation with TS_i that approximates the pulse shaping effect of the QIE slew rate as measured on a test bench.

The template fit is done with a non-negative least squares minimization algorithm [4] with

$$\chi^2 = \left(\sum A_i \vec{p_i} - \vec{q}\right)^{\mathrm{T}} \left(\Sigma_{\mathrm{d}} + \sum A_i^2 \Sigma_{p,i}\right)^{-1} \left(\sum A_i \vec{p_i} - \vec{q}\right) \tag{5}$$

where i runs over all possible pulses, A_i is the fitted pulse amplitude, $\vec{p_i}$ is the pulse shape template corresponding to the measured charge in the relevant TS, $\vec{q}$ is the observed data in each TS, Σ_{d} is the "dark" noise terms and $\Sigma_{p,i}$ is the pulse shape uncertainty.

The "dark" noise term is treated as fully uncorrelated between time slices. It includes the per-channel electronic noise as measured in pedestal runs, the uncertainty induced by the finite granularity of the ADC for the QIE chip in question, a photo-statistics term, and effects due to the SiPM dark current. A fully correlated uncertainty including the electronic noise and dark current terms are additionally imposed on the pedestal term.

The pulse shape uncertainty includes correlations between time slices, and is calculated using the nominal pulse shape template and 1σ variations and symmetrized over the positive and negative variations. The 1σ arrival time variations were measured in isolated bunch collisions by fitting the appropriate template with a floating arrival time (and amplitude) to individual

hits and calculating the standard deviation of the distribution. For the SiPM+QIE11 system, 1σ value was measured to be 2.5 ns, and for the HPD+QIE8, 5.0 ns.

The fit is initialized with a single pulse shape in the bunch-crossing of interest and a flat baseline component. If the result has an absolute $\chi^2 > 15$, the fit is repeated allowing for three pulses in the bunch crossing of interest, previous, and next, and a flat baseline term. In each case, all amplitudes are initialized as zero.

4. Results

In the following single channel fits in Figure 3, the data are shown as black dots. The uncertainty bars include the electronic noise, photo-statistics, and ADC granularity components. The black distribution is the total fit result. The red distribution is the in-time pulse which feeds into the global reconstruction. The light blue distributions are the fitted out-of-time pulses, and the grey dashed line is the fitted baseline. These plots illustrate the range of pileup configurations - a dominant in-time pulse, and dominant pulses in the next or previous collisions. In particular, the measured in-time charge Also one plot with the HPDs demonstrates the different pulse shape and relative gain of the SiPM+QIE11 vs HPD+QIE8 electronics.

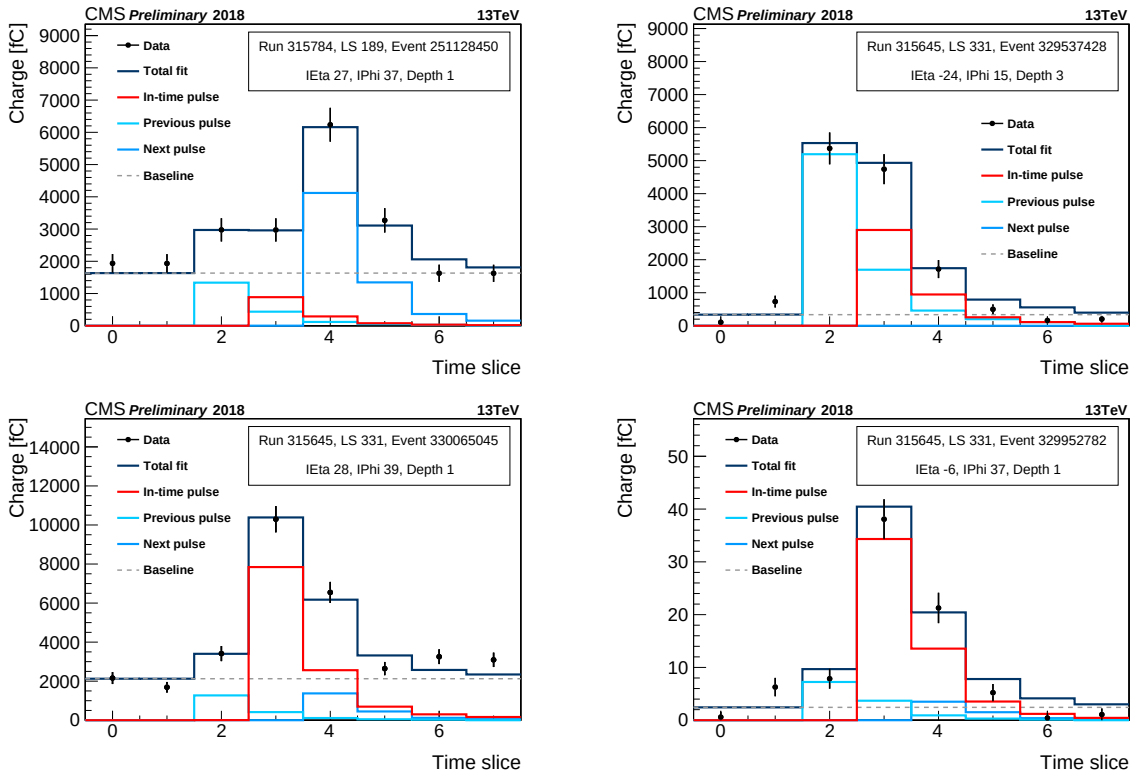

Figure 3. Example single channel fit results. The data and fit results are plotted per QIE time slice (TS), with the y axes in femtocoulomb. The black dots are data with electronics noise, photo-statistics, and ADC granularity uncertainties, and the black distribution is the total fit result. The red distribution is the fitted in-time pulse component, while the out-of-time components are light blue, and the baseline component is the dashed gray line. The bottom right plot is for an HPD+QIE8 channel in HB, all others are for SiPM+QIE11 channels in HE. The fits demonstrate the impact of OOTPU subtraction for channels dominated by either the previous bunch crossing (top right), or next bunch crossing (top left).

In Figure 4, the same single charged pion simulation sample, flat in pion energy between 50 and 100 GeV, is considered after digitization in two scenarios: no injected pileup, and with 50 pileup at 25 ns bunch spacing. The reconstructed energy response in each case is calculated as the ratio of reconstructed to simulated energy for each channel. Then the relative energy response is defined as the ratio of the energy response with pileup to the energy response without pileup. This variable demonstrates the impact of pileup on the energy response of HCAL, with higher relative energy response indicating larger pileup contamination. The OOTPU mitigation of the template fit reduces the pileup contamination by up to 25% in the lowest simulated energy bin (200 MeV to 500 MeV), which is a critical region for isolation quantities.

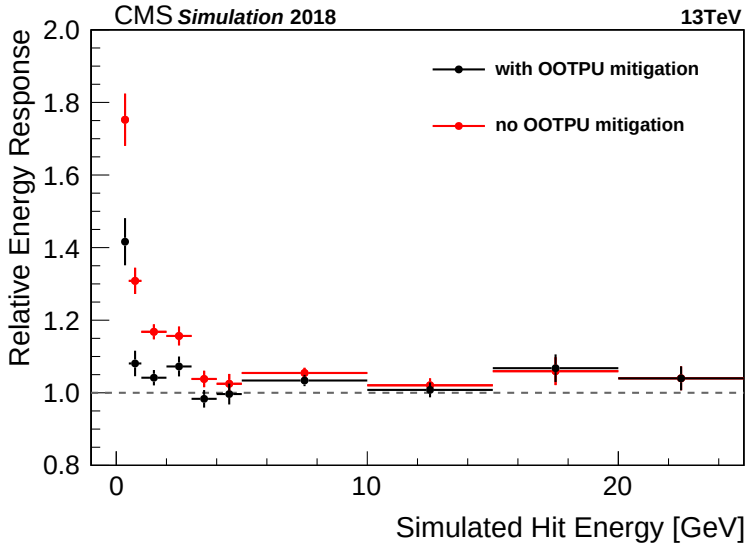

Figure 4. Relative energy response in simulation as a function of simulated hit energy. The reconstructed energy response in each case is calculated as the ratio of reconstructed to simulated energy for each channel. Then the relative energy response is defined as the ratio of the energy response with pileup to the energy response without pileup.

In Figure 5, the charged-hadron resolution in 0.5 pb^{-1} of early 2018 data for isolated tracks with $20 < p_T < 30$ GeV is plotted. The computed quantity is the measured HCAL energy E_{HCAL} divided by the track momentum p after correction for energy deposited in ECAL, E_{ECAL}. The track momentum is assumed to be the truth for this purpose. Further details are found in [5].

In the plot, the black points represent the distribution using OOTPU mitigation. The red points represent no OOTPU mitigation. The exact same events and objects are used in each case, however the no-mitigation scenario has a long tail with HCAL energy more than twice the measured track momentum not shown in this plot, which lowers the number of events shown in the chosen range.

A Gaussian fit is performed to each distribution, and σ is the resulting Gaussian width. The root-mean-square error (RMS) is calculated directly using the data points in each distribution, and includes the non-gaussian components of the resolution distribution. The most probable value (MPV) is also calculated directly from the distribution. The σ and RMS values are divided by the corresponding measured most probable value (MPV) to allow more direct comparison. The listed quantities consider the plotted region only. The OOTPU mitigation slightly improves the bulk resolution, and significantly reduces the over-estimated tail.

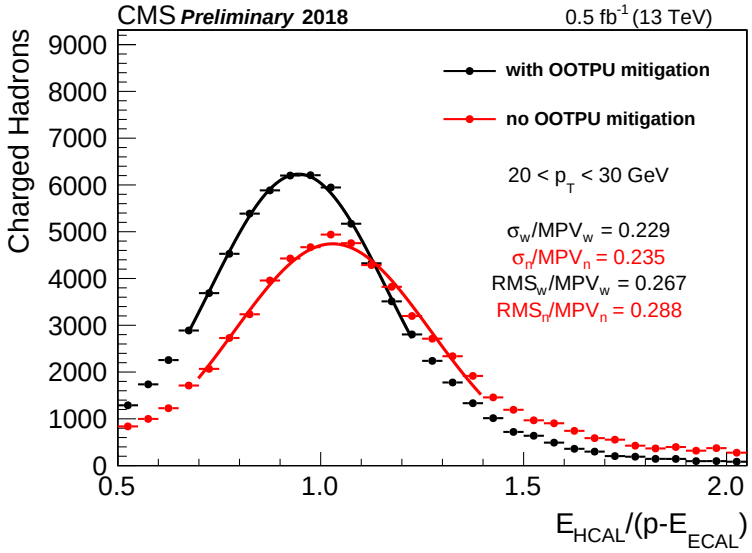

Figure 5. Distribution of response to charged hadrons with $20 < p_T < 30$ GeV in HBHE, with (black) and without (red) OOTPU mitigation. A Gaussian fit is performed to each distribution, and σ is the resulting Gaussian width. The root-mean-square error (RMS) is calculated directly using the data points in each distribution, and includes the non-Gaussian components of the resolution distribution. The σ and RMS values are divided by the corresponding measured most probable value (MPV). The listed quantities consider the plotted region only.

5. Conclusions

This represents an in situ pulse shape measurement with the full SiPM+QIE11 readout chain of scintillator tiles, Y11 fibers, SiPM optical detection and readout, QIE11 pulse shaping. Additionally, the 2018 OOTPU mitigation algorithm for the CMS hadronic detector barrel and endcap is described, and object-level performance metrics demonstrate the pileup contamination is reduced by up to 25% in the lowest simulated energy bin and a significant reduction in extremely overestimated hadronic energies for charged hadrons.

References

[1] CMS Collaboration 2008 *JINST* **3** S08004.
[2] CMS Collaboration 2010 *JINST* **5** T03013.
[3] CMS Collaboration 2017 CERN-CMS-DP-2017-042.
[4] Chen D and Plemmons R 2009 *The Birth of Numerical Analysis* (Singapore: World Scientific) pp 109–139.
[5] CMS Collaboration 2017 CERN-CMS-DP-2017-016.
[6] CMS Collaboration 2018 CERN-CMS-DP-2018-019.
[7] CMS Collaboration 2018 CERN-CMS-DP-2018-018.